Composite Structures 137 (2016) 18–32

Contents lists available at ScienceDirect

Composite Structures

journal homepage: www.elsevier.com/locate/compstruct

Multiscale modeling of macroscopic and microscopic residual stresses in metal matrix composites using 3D realistic digital microstructure models

X.X. Zhang [a], B.L. Xiao [a], Heiko Andrä [b], Z.Y. Ma [a,*]

[a] Shenyang National Laboratory for Materials Science, Institute of Metal Research, Chinese Academy of Sciences, 72 Wenhua Road, Shenyang 110016, China
[b] Fraunhofer Institute for Industrial Mathematics, Fraunhofer-Platz 1, Kaiserslautern 67663, Germany

ARTICLE INFO

Article history:

Keywords:
Multiscale modeling
Homogenization
Residual stress
Realistic microstructure
Boundary condition
RVE size

ABSTRACT

This work presents a hierarchical multiscale method for predicting accurately and efficiently the macroscopic and microscopic residual stresses (RSes) in MMCs based on large-size realistic digital microstructure models. Effects of various conditions on the multiscale modeling are systematically studied. Results indicate that the hierarchical multiscale model shows both a good self-consistency and a good accuracy. Compared with the kinematic uniform boundary conditions, the static uniform boundary conditions lead to more accurate prediction of the thermal misfit RS. The size of the volume element has significant effects on the predicted values of the thermal misfit RS. The hierarchical multiscale model gains significant advantages over the hybrid-semiconcurrent one with respect to both computational efficiency and computer memory cost. The local fluctuation profiles and total variations of the total RS are dominated by those of the thermal misfit RS at the microscale and by those of the macroscopic RS at the macroscale, respectively.

1. Introduction

Besides the macroscopic residual stress, significant microscopic residual stress inherently develops in metal matrix composites (MMCs) after thermo-elastoplastic deformation because of the differences in the elastic modulus, the plastic deformation ability and the coefficient of thermal expansion (CTE) between the reinforcement and the matrix. The residual stress in MMCs can be significantly negative for the properties of MMCs [1–9]. For instance, the tensile residual stress in the matrix encourages the micro-crack initiation [5], accelerates the fatigue crack growth rate [7,8] and reduces the threshold of maximum stress intensity factor [9]. Besides, residual stress can be a major factor in dimension instability and cause serious problem for reliable precision devices [10].

To guarantee high-performance, reliability and safety of engineering design, quantitative knowledge of the residual stress is critical. Nonetheless, both measurements and predictions of the residual stress in MMCs are historically difficult [1], because both the macroscopic and microscopic residual stresses are presented [11,12].

Non-destructive methods for determining the residual stress like the neutron diffraction and the synchrotron X-ray diffraction are experimentally difficult and costly job [11,13]. Especially, they suffer from inaccurate measurements of the unstrained reference lattice parameters of aging-hardened matrices in MMCs [11,12,14].

Quantitatively computing residual stress distributions are alternative methods for evaluating the residual stress in MMCs. In the past, the Eshelby method was applied to calculate the microscopic residual stress in MMCs [11,15–17], which, however, has several shortcomings because a lot of assumptions are made [11,17]. Besides the Eshelby method, the unit cell based finite element method (FEM) is often used on the microscale to predict the thermal misfit residual stress in MMCs [18–22]. However, a crucial issue of the unit cell FEM is that it only deals with the microscopic residual stress with the macroscopic residual stress being ignored.

Multiscale modeling is an arising new tool to study both the macroscale and microscale behaviors of MMCs [23–28]. One main advantage of multiscale modeling is that complicated initial and boundary conditions at the macroscale can be studied for real-life engineering problems [23,25], e.g. heat treatments, welding and forming processes. Meanwhile, it enables one to investigate the effects of the microscale features, such as complex microstructure, inter- and intra-phase interactions, and interface properties. In addition, it shares both the efficiency of the

* Corresponding author. Tel./fax: +86 24 83978908.
E-mail address: zyma@imr.ac.cn (Z.Y. Ma).

http://dx.doi.org/10.1016/j.compstruct.2015.10.045
0263-8223/

Nomenclature

δ	size ratio of microstructure domain
L	side length of microstructure domain
D	mean diameter of particles
Ω	macroscale domain
ω	microscale domain/volume element
σ	stress tensor
ε	strain tensor
$\boldsymbol{u}$	displacement vector
$\boldsymbol{t}$	traction vector
$\boldsymbol{n}$	normal vector of boundary surface
$\boldsymbol{x}$	coordinate vector of boundary nodes
Superscripts I, II	types of microscale thermo-mechanical models
Scripts M, m	M denotes macroscale or macroscopic, and m microscale or microscopic
Superscripts ep, th, eM, tM	ep denotes elasto-plastic, th thermal, eM elastic mismatch, tM thermal misfit
Superscripts β, ma and pa	β denotes ma or pa, ma denotes matrix and pa particle
Subscripts i	denotes xx, yy or zz which are tensor component index
$\langle\cdot\rangle$	volume average function

macroscale model and the accuracy of the microscale model [26]. Therefore, multiscale modeling provides an excellent method to deeply understand the inherent physics of the multiscale mechanics under external boundary conditions for MMCs.

In the multiscale modeling, the coupling methods by which the microscale model is connected to the macroscale model can be classified into two basic types [26,29–31]: concurrent and hierarchical (also referred to sequential or serial) methods. Besides these two basic methods, several other methods fall in the area between them, e.g. the semiconcurrent and the hybrid-semiconcurrent methods [30]. In general, compared with the hierarchical method, the concurrent method does not need explicit macroscale constitutive model for the macroscale problem. However, the computational cost of the concurrent method is higher than that of the hierarchical method. Up to now, several multiscale models based on different coupling methods were proposed to investigate the multiscale mechanics of MMCs.

For instance, Ghosh et al. [32] developed a hierarchical multiscale method for elasto-plastic analysis of heterogeneous materials (including MMCs). Feyel [33] developed a concurrent multiscale method, called FE^2 method, for mechanical analysis of heterogeneous materials. Later, Özdemir et al. [34] developed a FE^2 method for thermo-mechanical analysis of heterogeneous materials. Nonetheless, little work has yet been conducted on applying multiscale modeling to predict both the macroscopic and microscopic residual stresses in MMCs.

Recently, Zhang et al. [31] developed a hybrid-semiconcurrent multiscale model to compute both the macroscopic and microscopic residual stresses in MMCs. The predicted residual stresses in quenched MMC [31] agreed reasonably well with the reported experimental results [11]. Nonetheless, this multiscale model was based on the unit cell model and hybrid-semiconcurrent coupling method. The accuracy and the efficiency of this multiscale model need to be improved due to the following reasons.

First, the unit cell model ignores the random shape, size and spatial distributions of the reinforcement [31,35]. Second, the unit cell model based homogenization models introduce considerable errors in the predicted effective material properties of MMCs [35–40]. If these effective material properties are used in the macroscale model, then errors are introduced in the predicted residual stresses of MMCs [31]. Third, the computational costs of the concurrent, semiconcurrent and hybrid-semiconcurrent methods are relatively expensive [30].

Therefore, there is a strong demand to develop multiscale models which predict accurately and efficiently the macroscopic and microscopic residual stresses in MMCs using the realistic digital microstructure models. The preset work aims at developing a hierarchical multiscale method to satisfy these demands. The effects of various conditions on the multiscale predictions are systematically studied. These conditions include: (i) the multiscale coupling methods, (ii) the types of macro–micro scale transition boundary conditions, and (iii) the domain sizes of microstructures. As an application of this hierarchical multiscale model, the residual stresses developed during the quenching process of a 3 μm 17 vol.% SiCp/2124Al composite are studied.

2. Theory of the multiscale model

2.1. The multiscale model

The general 3D multiscale thermo-mechanical framework for multiphase materials has been reported in the previous study [31] and is applied in this work. The main ideas of the framework are summarized in the following.

At the macroscale, the governing equations for heat flow and mechanical equilibrium need to be solved with respect to the initial and boundary conditions corresponding to real engineering problems. MMC is assumed as a continuum media at the macroscale and is described by a J_2-flow theory of infinitesimal thermo-elastoplasticity [41] based on the pre-computed effective properties via computational homogenizations [40].

At the microscale, the temperature is assumed to be constant in each volume element corresponding to the macroscale integration point P. Each phase in MMCs is described by a J_2-flow theory of infinitesimal thermo-elastoplasticity [41]. For rigid ceramic reinforcement that normally undergoes only elastic deformation, the yield stress of the reinforcement is set to a sufficient large number.

2.2. Separation of residual stresses and macro–micro scale transition boundary conditions

Separation of different contributions to the total residual stresses offers deep insight to the residual stress in the MMCs. In many experimental/industrial cases, because of inaccurate measurements of the unstrained parameters of the matrix (d_0 problem), direct measurements/calculations of the total residual stresses will lead to significant errors [11]. In such cases it is important to measure various contributions first and then add them together to get the total residual stresses, as shown in [12]. Such experimental procedure requires corresponding modeling procedure. Besides, if different contributions of the total residual stresses are addressed, the results can be used as a guide to select the best kind of reinforcement with respect to optimization of the total residual stresses. Because the elastic mismatch residual stress is mainly controlled by the difference in the elastic properties between the matrix and the reinforcement, whereas the thermal misfit residual stress is mainly controlled by the difference in the CTE between the phases.

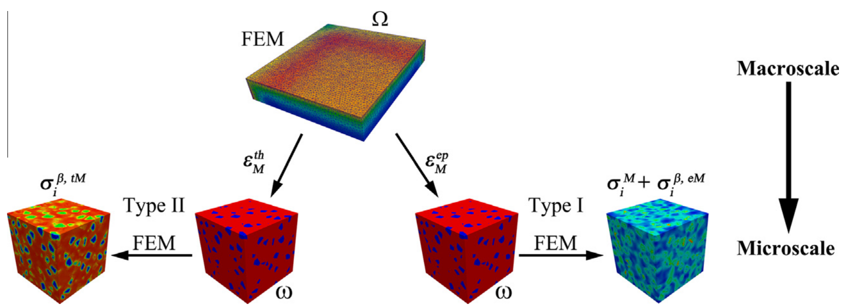

Fig. 1. Schematic representation of the hierarchical multiscale model.

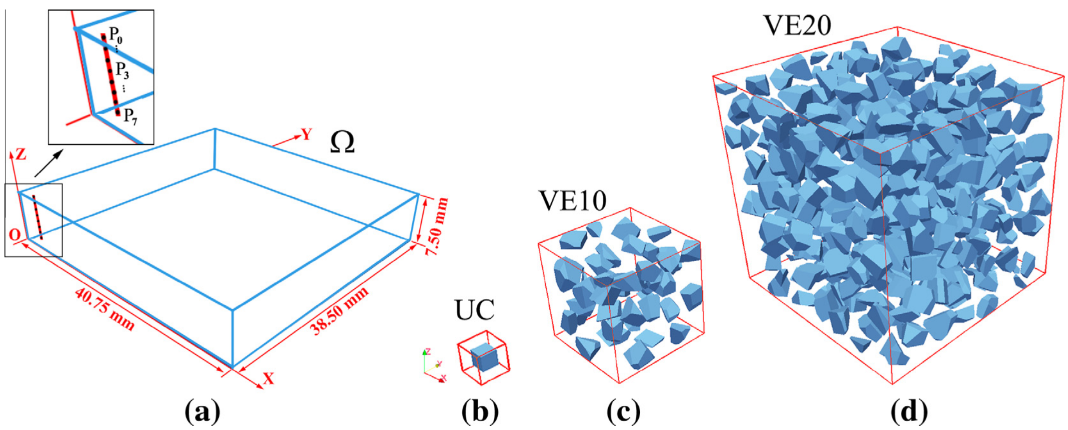

Fig. 2. Geometry models used in the multiscale models: (a) one-eight of the MMC plate. $\overline{XOY}$, $\overline{XOZ}$ and $\overline{YOZ}$ planes are imposed by symmetrical displacement boundary conditions. (b) Unit cell model UC with size ratio $\delta \approx 1$, (c) realistic microstructure model VE10 with $\delta = 10$, 44 random particles, (d) realistic microstructure model VE20 with $\delta = 20$, 408 random particles. The mean diameter of particles is 3 μm for all microstructures.

In the present work, two types of macro–micro scale transition boundary conditions, i.e. the kinematic uniform boundary conditions (KUBC), the static uniform boundary conditions (SUBC), are investigated to assess their influences. Two types of microscale models are constructed for separating the different microscopic residual stresses [31].

The KUBC for type I microscale thermo-mechanical model that calculates the macroscopic and elastic mismatch residual stresses $\langle\sigma_i^M\rangle$ and $\langle\sigma_i^{\beta,eM}\rangle$ is defined by

$$\boldsymbol{u}_m^I = \boldsymbol{\varepsilon}_M^{ep} \cdot \boldsymbol{x}_m \qquad (1)$$

Definitions of all symbols are listed and explained in Nomenclature.

The KUBC for type II microscale thermo-mechanical model that calculates the thermal misfit residual stress $\langle\sigma_i^{\beta,tM}\rangle$ is defined by

$$\boldsymbol{u}_m^{II} = \boldsymbol{\varepsilon}_M^{th} \cdot \boldsymbol{x}_m \qquad (2)$$

The SUBC for type II microscale thermo-mechanical model that calculates the thermal misfit residual stress $\langle\sigma_i^{\beta,tM}\rangle$ is defined by

$$\boldsymbol{t}_m^{II} = \boldsymbol{0} \cdot \boldsymbol{n}_m \qquad (3)$$

2.3. Numerical solution method

The hierarchical coupling method is applied to reduce computational effort for solving the multiscale problem. In the hierarchical multiscale model, the macroscale thermo-mechanical model is solved independently of type I microscale thermo-mechanical model. The residual vector and the tangent stiffness matrix for all the macroscale finite element (FE) integration points are computed via the pre-computed macroscale constitutive model.

For the purpose of comparison, new results of the hybrid-semiconcurrent multiscale model reported in the previous work [31] are also investigated. In the hybrid-semiconcurrent multiscale model, the macroscale thermo-mechanical model and type I microscale thermo-mechanical model are solved simultaneously at the macroscale FE integration points for solving the macroscale and elastic mismatch residual stresses. The residual vector and the tangential stiffness matrix at the macroscale FE integration points are homogenized via type I microscale thermo-mechanical model.

The illustration of the hierarchical multiscale model is shown in Fig. 1. To assess the accuracy and efficiency of the hierarchical coupling method, the unit cell based hybrid-semiconcurrent multiscale model (see [31]) is compared to the hierarchical multiscale model using the same unit cell.

3. Numerical experiments

As an application of this multiscale model, the residual stresses developed during the quenching process from 505 to 25 °C for a 3 μm 17 vol.% SiC_p/2124Al composite are studied. Due to the symmetry of the problem, one eighth of the macroscale geometry is taken as computational domain Ω, which is shown in Fig. 2(a).

Volume elements of realistic microstructure models are considered. Details about generating 3D realistic microstructure models have been reported previously [31,42]. To assess the effects of the size of the volume elements ω, different sizes are investigated. Here the size ratio δ of a volume element is defined by

$$\delta = 2L/D \qquad (4)$$

Table 1
Explanation of abbreviations for hierarchical and hybrid-semiconcurrent multiscale models.

				MICRO1				MICRO2			
				Coupling method	Transition boundary condition	Microstructure model	Point	Coupling method	Transition boundary condition	Microstructure model	Point
MULTI	=	MACRO	+	HS	KUBC	UC	P0				
				HS	KUBC	UC	P1				
				HS	KUBC	UC	P2				
				HS	KUBC	UC	P3				
				HS	KUBC	UC	P4				
				HS	KUBC	UC	P5				
				HS	KUBC	UC	P6	HE	KUBC	UC	P7
				HS	KUBC	UC	P7	HE	SUBC	UC	P7
MULTI	=	MACRO	+	HE	KUBC	UC	P0				
				HE	KUBC	UC	P1				
				HE	KUBC	UC	P2				
				HE	KUBC	UC	P3				
				HE	KUBC	UC	P4				
				HE	KUBC	UC	P5				
				HE	KUBC	UC	P6				
				HE	KUBC	UC	P7	HE	SUBC	UC	P7
MULTI	=	MACRO	+	HE	KUBC	VE10	P0				
				HE	KUBC	VE10	P1				
				HE	KUBC	VE10	P2				
				HE	KUBC	VE10	P3				
				HE	KUBC	VE10	P4				
				HE	KUBC	VE10	P5				
				HE	KUBC	VE10	P6				
				HE	KUBC	VE10	P7	HE	SUBC	VE10	P7
MULTI	=	MACRO	+	HE	KUBC	VE20	P0				
				HE	KUBC	VE20	P1				
				HE	KUBC	VE20	P2				
				HE	KUBC	VE20	P3				
				HE	KUBC	VE20	P4				
				HE	KUBC	VE20	P5				
				HE	KUBC	VE20	P6				
				HE	KUBC	VE20	P7	HE	SUBC	VE20	P7

Notation explanation. MACRO: macroscale model; MACRO1: type I microscale model; MACRO2: type II microscale model; coupling method $\in$ {HS, HE}, HS: hybrid-semiconcurrent method, HE: hierarchical method; transition boundary condition $\in$ {KUBC, SUBC}, KUBC: kinematic uniform boundary conditions, SUBC: static uniform boundary conditions; microstructure model $\in$ {UC, VE10, VE20}, UC: unit cell model, VE10: volume element with size ratio 10; VE20: volume element with size ratio 20; point $\in$ {P0,...,P7}, definitions of points are list in Table 2.

The unit cell is also investigated for comparison. The circumscribed spheres of particles have a mean diameter of 3 μm. All microstructure models are shown in Fig. 2. The unit cell model with size ratio $\delta \approx 1$ is named as UC; the 3D realistic microstructure models with size ratio δ being 10 and 20 are named VE10 and VE20, respectively.

In the present paper, the hierarchical and hybrid-semiconcurrent multiscale models are tagged with MULTI(coupling method, microstructure model). The macroscale models are tagged with MACRO(coupling method, microstructure model). Type I microscale models are tagged with MICRO1(coupling method, microstructure model, points). Type II microscale models are tagged with MICRO2(transition boundary condition, microstructure model, points). The notations of coupling method, transition boundary condition, microstructure model and points are listed in Table 1. The macroscale coordinates $\vec{\mathbf{X}}$ of eight points for multiscale models are listed in Table 2 and illustrated in Fig. 2(a).

Table 2
Macroscale coordinates $\vec{\mathbf{X}}$ of eight points for multiscale models.

Points	Coordinates $\vec{\mathbf{X}}$, mm		
	X	Y	Z
P_0*	1.91	0.58	7.38
P_1	1.91	0.65	6.35
P_2	1.77	0.37	5.42
P_3	1.49	0.24	4.47
P_4	1.76	0.63	2.95
P_5	1.96	0.34	2.03
P_6	1.74	0.54	1.17
P_7**	1.79	0.67	0.18

* Near the top surface of the real MMC plate.
** Near the center of the real MMC plate. In the one eighth structure, P_7 is near the bottom boundary face.

The temperature dependent material properties for 2124Al (Young's modulus, Poisson's ratio, yield strength, ultimate strength, and CTE) [40,43] and SiC (Young's modulus, Poisson's ratio, and CTE) [44] are used, as the same in the previous studies [31,40]. The effective constitutive model of the 3 μm 17 vol.% SiC_p/2124Al composite at the macroscale are determined using the computational homogenization technique [40].

In the present work, all domains at both the macroscale and the microscale are meshed by unstructured tetrahedrons with 4-nodes by the Delaunay triangulation software TetGen [45]. Linear shape functions are used. All the multiscale simulations are carried out in MSFESL [31,40,42]. The reported experimental results [11] are used to compare with the predictions.

4. Results and discussions

4.1. Temperature and cooling rate

The different temperature curves of points P_0 and P_7 shown in Fig. 3(a) indicates that temperature gradient (inhomogeneous tem-

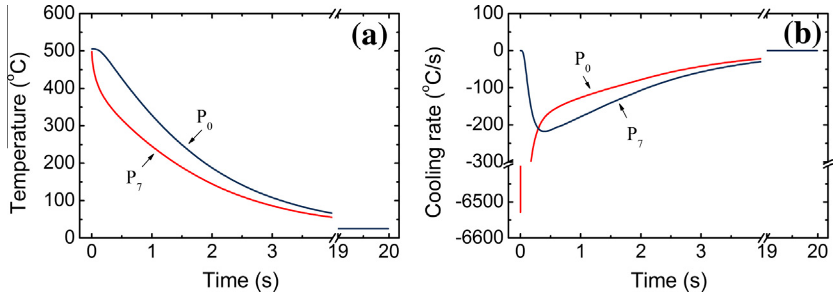

Fig. 3. Temperature (a) and cooling rate (b) at points P_0 and P_7.

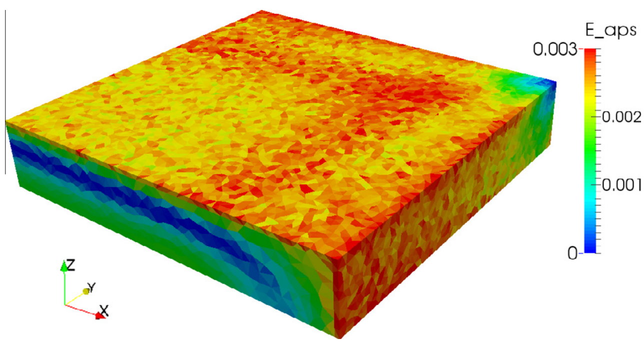

Fig. 4. Macroscopic accumulated plastic strain field computed via MACRO(HE, VE20).

perature distribution) exists during the whole quenching process. Besides, the different cooling rates of points P_0 and P_7 shown in Fig. 3(b) reveals that the MMC plate has a gradient of cooling rate.

4.2. Plastic deformation

The inhomogeneous temperature distribution and the heterogeneous cooling rate cause inhomogeneous deformation in the MMC plate. As a result, internal stresses in the MMC plate are generated [46]. When the internal stress exceeds the yield strength, plastic deformation occurs and the internal stress is partly relaxed.

Fig. 4 shows the macroscopic accumulated plastic strain field computed via the macroscale model MACRO(HE, VE20), in which the MMC is modeled by a homogeneous material and described by J_2-elastoplastic theory [31,40]. Therefore, the macroscopic accumulated plastic strain field corresponds to the effective material of the MMC [31,40]. The macroscopic plastic deformation introduces additional residual stress which reduces the macroscopic residual stress [17,47].

Fig. 5(a) and (b) show that the microscopic plastic deformation in the matrix, caused by both the macroscopic temperature gradient and the mismatch in elastic constants between the phases, respectively, is roughly homogeneous in the volume element. This plastic deformation causes relaxation of both the macroscopic and elastic mismatch residual stresses [17,47]. Fig. 5(c) shows that the microscopic plastic deformation in the matrix, caused by the mismatch in the CTE between the phases, has large gradient. The plastic deformation on or near the matrix/particle interface is much larger than that away from the interface. This plastic deformation causes relaxation of the thermal misfit residual stress [17,47]. It also leads to high dislocation density near the matrix/particle interface [48–50]. Fig. 5(a)–(c) show that the plastic deformation near the matrix/particle interface is mainly caused by the mismatch in the CTE between the phases.

4.3. Macroscopic residual stress

Fig. 6 shows that the evolutions of the macroscopic residual stresses predicted via macroscale models MACRO(HE, UC) and MACRO(HE, VE20) are close, except a little difference at the beginning of the quenching process (e.g. before 1.0 s).

Fig. 7 shows that the macroscopic residual stresses predicted directly via different macroscale models and homogenized via different microscale models are very close. This is important because it proves the self-consistency of the hierarchical coupling method. Meanwhile, the predicted profiles of the macroscopic residual stress in the MMC in this study agree quite well with the results from reference [51].

Fig. 7(a) shows that the predicted total variations of σ_{xx}^M across the thickness of the MMC plate are: ∼233 MPa homogenized via MICRO1(HS, UC, P_{0-7}), ∼231 MPa homogenized via MICRO1(HE, UC, P_{0-7}), and ∼236 MPa computed via MACRO(HE, UC). It can be seen that the hierarchical multiscale model MULTI(HE, UC) gives almost the same homogenized macroscopic residual stress as the hybrid-semiconcurrent multiscale model MULTI(HS, UC). Fig. 7(a) also shows that the larger domain size of the microstructure, the larger total variation of σ_{xx}^M across the thickness. It clearly shows that the predicted total variation of σ_{xx}^M across the thickness of the MMC plate agrees very well with the experimental result

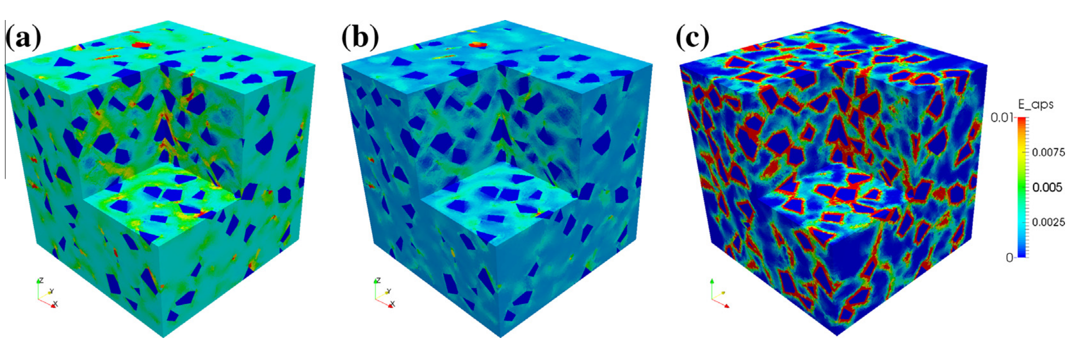

Fig. 5. Microscopic accumulated plastic strain fields computed via MICRO1(HE, VE20, P_0) (a), MICRO1(HE, VE20, P_7) (b), MICRO2(KUBC, VE20, P_7) (c).

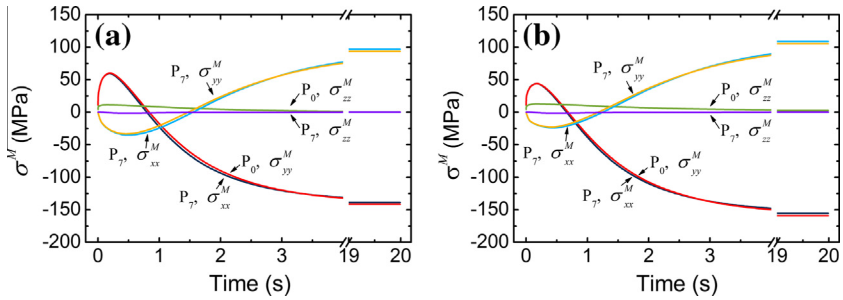

Fig. 6. Comparison of the evolutions of macroscopic residual stresses that are computed via MACRO(HE, UC) (a) and MACRO(HE, VE20) (b).

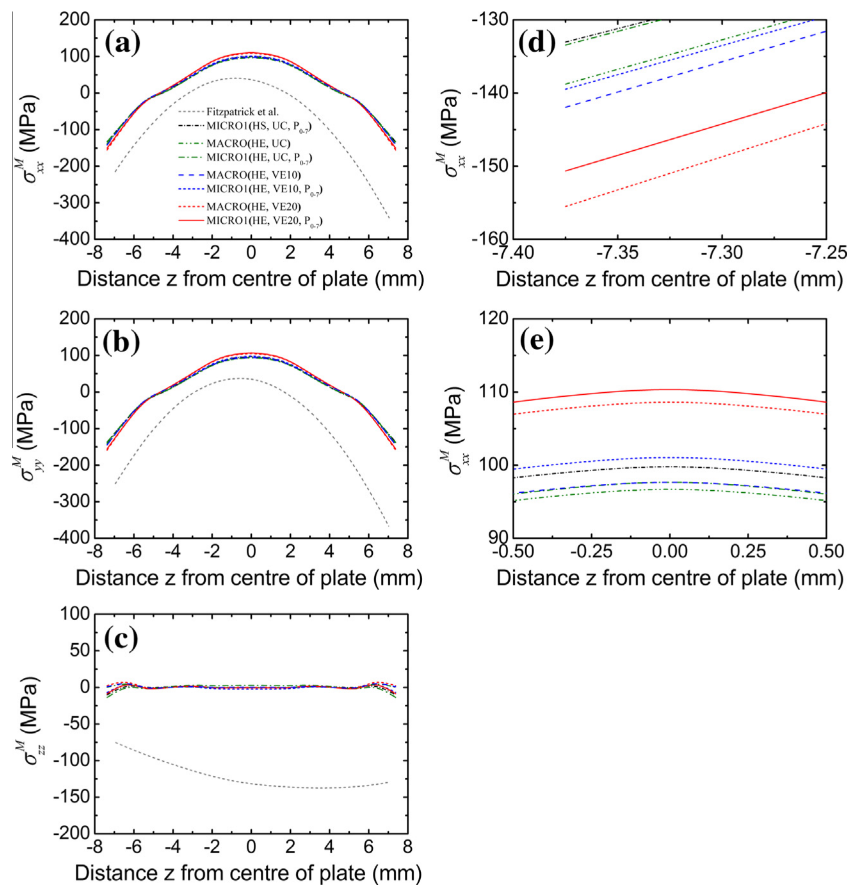

Fig. 7. Comparison between the computed macroscopic residual stresses from different macroscale models, the homogenized macroscopic residual stresses from different microscale models and the determined ones via Eshelby model from Fitzpatrick et al. [11].

[11]: ~261 MPa homogenized via MICRO1(HE, VE20, P_{0-7}), ~264 MPa computed via MACRO(HE, VE20, P_{0-7}), and ~259 MPa measured in [11] across the half thickness from −7.5 to 0 mm.

Fig. 7(a) shows that the relative deviation about the total variation of the predicted macroscopic residual stress component *xx* across the thickness of the MMC plate between the UC based and VE20 based hierarchical multiscale models is about $|233-261|/261 \times 100\% \approx 10.7\%$. Therefore, to obtain more accurate predictions of the macroscopic residual stress, large sized realistic microstructure should be used.

Fig. 7 shows that the experimental macroscopic residual stresses [11] are translated into compressive by about 100 MPa because of the inaccurate measurements of the "unstrained reference parameter" d_0 and the numerical fitting errors during the data processing [11,31]. This problem demonstrates that using multiscale modeling method for predicting the residual stress in MMCs is fundamentally important.

4.4. Elastic mismatch residual stress

Fig. 8(a)–(f) show that the profiles of the homogenized elastic mismatch residual stress components $\langle\sigma^{\beta,eM}_{xx}\rangle$, $\langle\sigma^{\beta,eM}_{yy}\rangle$ and $\langle\sigma^{\beta,eM}_{zz}\rangle$ across the thickness of the MMC plate predicted via MICRO1(HE, UC, P_{0-7}) are almost the same as those predicted via MICRO1(HS, UC, P_{0-7}). With the hierarchical coupling method, the larger domain size of the realistic microstructure, the larger total variations of $\langle\sigma^{\beta,eM}_{xx}\rangle$ and $\langle\sigma^{\beta,eM}_{yy}\rangle$ across the thickness of the MMC plate. For instance, the predicted total variation of $\langle\sigma^{\mathrm{ma},eM}_{xx}\rangle$ in the matrix via either MICRO1(HE, UC, P_{0-7}) or MICRO1(HS, UC, P_{0-7}) is

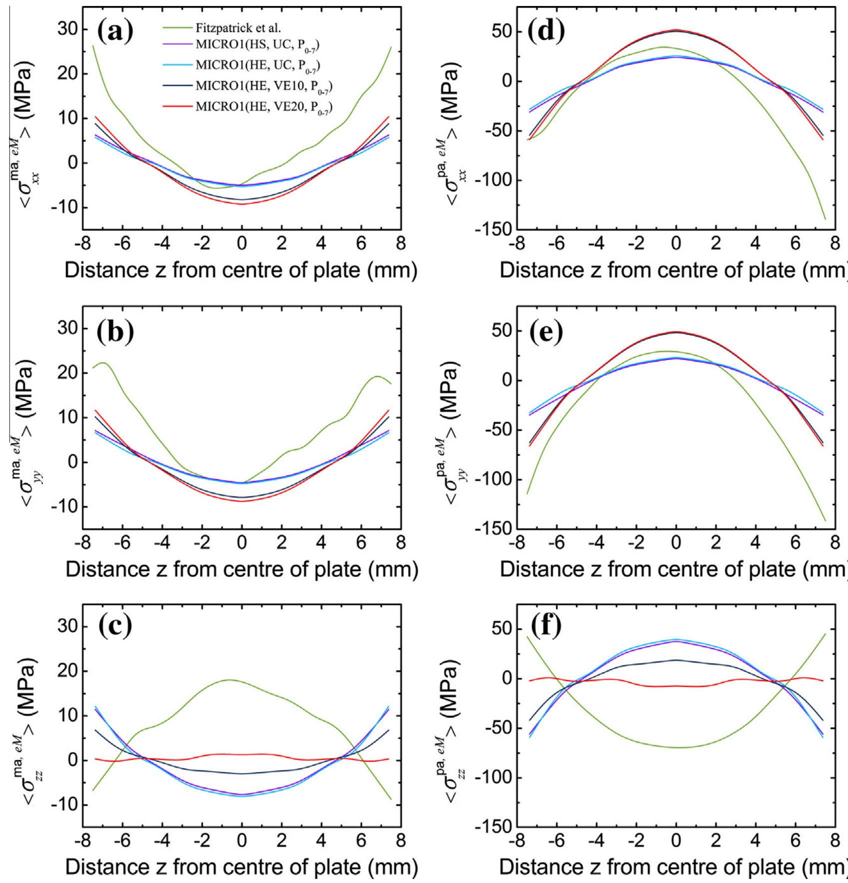

Fig. 8. Comparison between homogenized elastic mismatch residual stresses using different microscale models and determined ones via Eshelby model from Fitzpatrick et al. [11] in 2124Al (a)–(c) and SiC (d)–(f).

∼11 MPa, and that via MICRO1(HE, VE20, P_{0-7}) is ∼20 MPa. It can be seen that the UC based multiscale model greatly underestimates the total variations of the homogenized elastic mismatch residual stress components $\langle\sigma_{xx}^{\beta,eM}\rangle$ and $\langle\sigma_{yy}^{\beta,eM}\rangle$ across the thickness of the MMC plate.

Fig. 8(c) and (f) show that $\langle\sigma_{zz}^{\beta,eM}\rangle$ predicted via MICRO1(HE, VE20, P_{0-7}) are about zero across the thickness of the MMC plate and show much less variations, as one expected [11]. However, the ones predicted based on UC and VE10 are not. Fig. 8 (c) and (f) also show that the profiles of $\langle\sigma_{zz}^{\beta,eM}\rangle$ determined via Eshelby model [11] are opposite to those of $\langle\sigma_{zz}^{\beta,eM}\rangle$ predicted based on UC and VE10. Several facts may contribute to this inconsistency.

First, in the modeling, the cooling convection boundary conditions are imposed simultaneously to the surfaces that are contacted with the quenching medium (QM), e.g. water. However, in real experiments or manufacturing processes, the plates were drop into the QM. This means the surfaces of the plate were contacted with the QM gradually, although the whole quenching process is very fast. The part that was not in the QM (it has not shrunk too much) caused constraint to the part that was in the QM (it shrunk significantly due to quick cooling). This additional constraint was not considered in the model.

Second, the macroscopic (homogenized/effective) thermo-elastoplastic properties predicted via the UC and VE10 include large errors, especially via the UC [40]. These errors cause a further error in the computation of macroscale model (with respect to the macroscopic strain and stress). As a result, the microscopic elastic mismatch residual stress includes large errors, because the boundary conditions of the microscale model were constructed using the macroscopic strain.

Third, significant errors were included in the experimental results due to data fitting process and the d_0 problem [11]. These experimental errors have also affected the determined elastic mismatch residual stress. Therefore, in order to obtain accurate experimental data, it is better to perform a measurement system analysis that needs more measured residual strain/stress results.

Fig. 9 shows the elastic mismatch residual stress fields for both P_0 and P_7. It can be seen that the images of $\sigma_{xx}^{\beta,eM}$ and $\sigma_{yy}^{\beta,eM}$ fields are similar to each other, as shown in Fig. 9(a) and (e), (b) and (f), (c) and (g), (d) and (h). Fig. 9(a)–(l) show that the sign of $\sigma_i^{ma,eM}$ and $\sigma_i^{pa,eM}$ in many areas on or near the matrix/particle interface is opposite to its average nature.

Fig. 9 also shows that the sign of $\sigma_i^{ma,eM}$ and $\sigma_i^{pa,eM}$ on or near the boundary surfaces of MICRO1(HE, VE20, P_0) and MICRO1(HE, VE20, P_7) is opposite to its average nature. For instance, in Fig. 9(b), $\sigma_{xx}^{pa,eM}$ in most part of particles is compressive, but $\sigma_{xx}^{pa,eM}$ on or near the boundary surfaces of MICRO1(HE, VE20, P_0) is tensile (red color). Such a phenomenon is believed to be caused by the boundary condition effects. On the one hand, the boundary conditions of microscale models are the KUBC which are constructed using the macroscopic elastoplastic strain, see Eq. (1). The KUBC forces the boundary surfaces to remain flat during deformation. This undesirable constraint pollutes the residual stress results on the boundary surfaces [52]. On the other hand, with a low content of reinforcement, the MMCs behave similarly to that of their metal matrix. Therefore the magnitude of the macroscopic elastoplastic strain of the MMC plate is close to that of the elastoplastic strain of the metal matrix, but is significantly higher than that of the elastic strain of the ceramic particles. Consequently, when the boundary conditions are set via Eq. (1), the boundary nodes of the ceramic

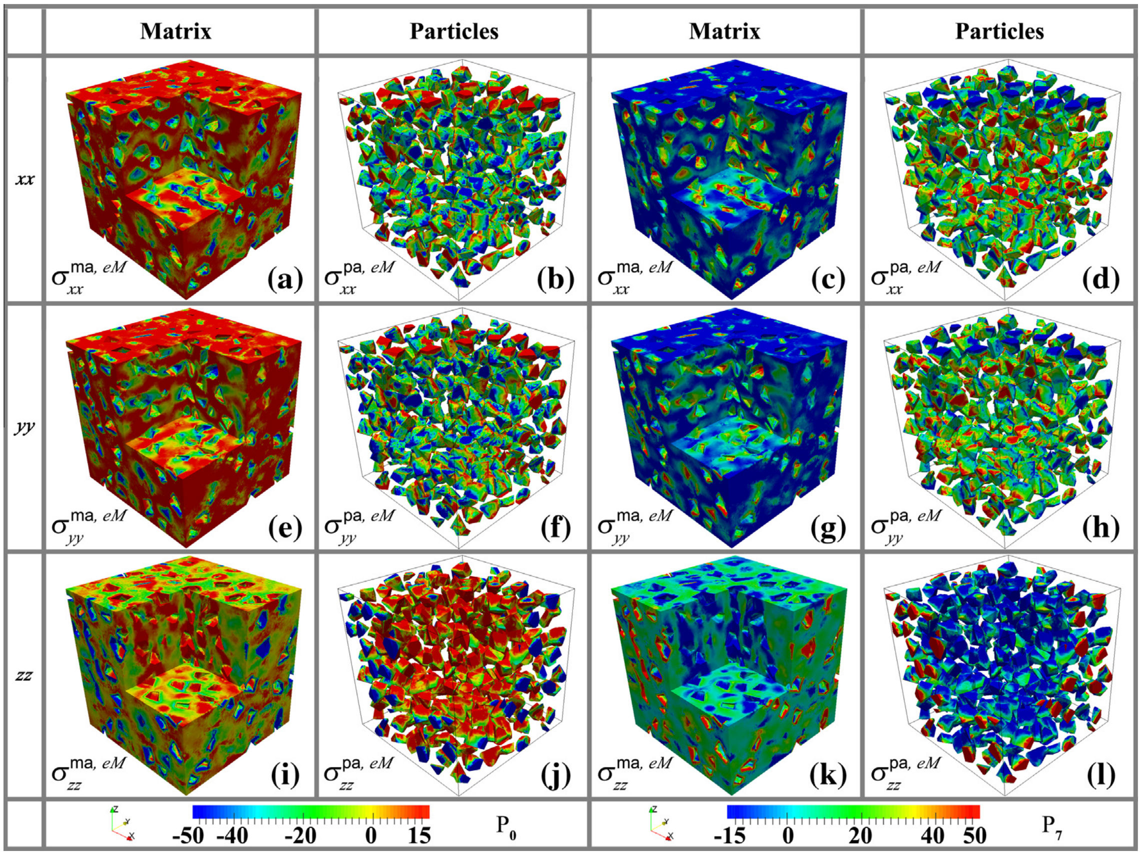

Fig. 9. Elastic mismatch residual stress fields computed based on VE20: the left two rows, i.e. (a), (b), (e), (f), (i) and (j), are the elastic mismatch residual stress fields are computed via MICRO1(HE, VE20, P_0); the right two rows, i.e. (c), (d), (g), (h), (k) and (l), are the total stress fields are computed via MICRO1(HE, VE20, P_7). For P0, the stress that is smaller than −50 MPa is also shown by blue color, and the stress that is larger than 15 MPa is also shown by red color. For P_7, the stress that is smaller than −15 MPa is also shown by blue color, and the stress that is larger than 50 MPa is also shown by red color. (For interpretation of the references to color in this figure legend, the reader is referred to the web version of this article.)

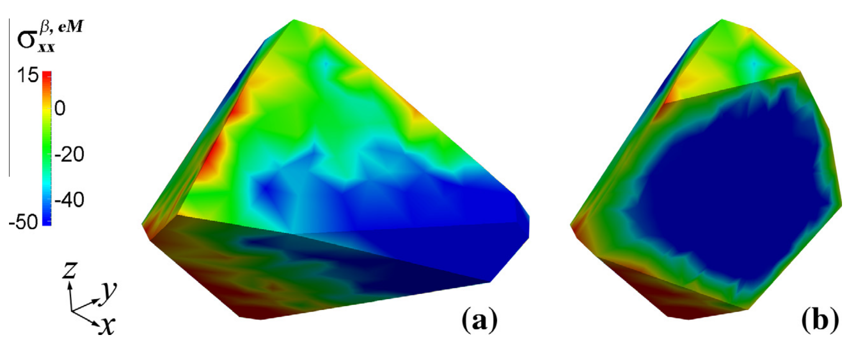

Fig. 10. Elastic mismatch residual stress $\sigma_{xx}^{\beta,eM}$ of a particle, which is from Fig. 8(b), computed via microscale model P_0: (a) map of the particle surface, (b) cut-view of the same particle.

particles are forced to deform as the same magnitude as the ones of the metal matrix, which leads to undesirable deformation of particles on the boundary surfaces.

Fig. 9 also shows that the sign of different components of elastic mismatch residual stress in MICRO1(HE, VE20, P_7) is more or less inverse of those in MICRO1(HE, VE20, P_0). This is easy to understand because of the distribution of the macroscopic residual stress as shown in Fig. 7.

To obtain clearer view of the stress fields of $\sigma_{xx}^{pa,eM}$, a particle in MICRO1(HE, VE20, P_0) is zoomed in Fig. 10. To obtain the exact values at different position, the elastic mismatch residual stress components along the line $\overline{AB}$ that are computed via MICRO1(HE, UC, P_0) and those along the line $\overline{CD}$ that are computed via MICRO1 (HE, VE20, P_0) are shown in Fig. 11. The lines $\overline{AB}$ and $\overline{CD}$ are defined in Fig. 12.

Fig. 11 shows that the microscale profiles of $\sigma_i^{\beta,eM}$ differ significantly from each other. This reveals that the elastic mismatch residual stress in the x–y plane has significant local anisotropy at the microscale. This is surprising because at the macroscale the elastic mismatch residual stress field in the X–Y plane is approximately isotropic as shown in Fig. 8, and from a statistical view the elastic mismatch residual stress field in the X–Y plane is also near isotropic as shown in Fig. 9.

Survey of Fig. 11(a) and (b) indicates that the variation trend and nature of $\sigma_i^{\beta,eM}$ computed based on UC (e.g. MICRO1(HE, UC, P_0)) are similar across the line $\overline{AB}$, i.e. in both phases. In fact,

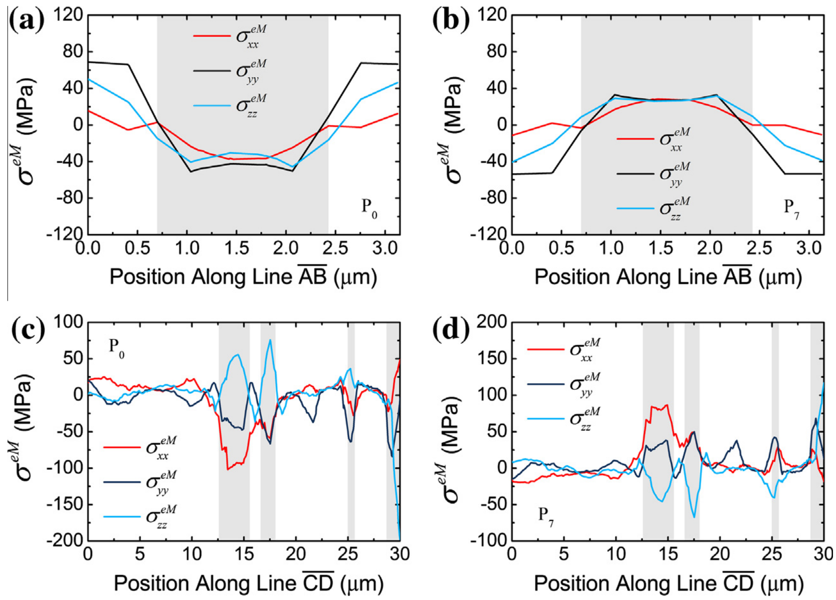

Fig. 11. Elastic mismatch residual stress components computed via different microscale models along lines $\overline{AB}$ and $\overline{CD}$ defined in Fig. 12: (a) MICRO1(HE, UC, P_0), (b) MICRO1 (HE, UC, P_7), (c) MICRO1(HE, VE20, P_0), (d) MICRO1(HE, VE20, P_7).

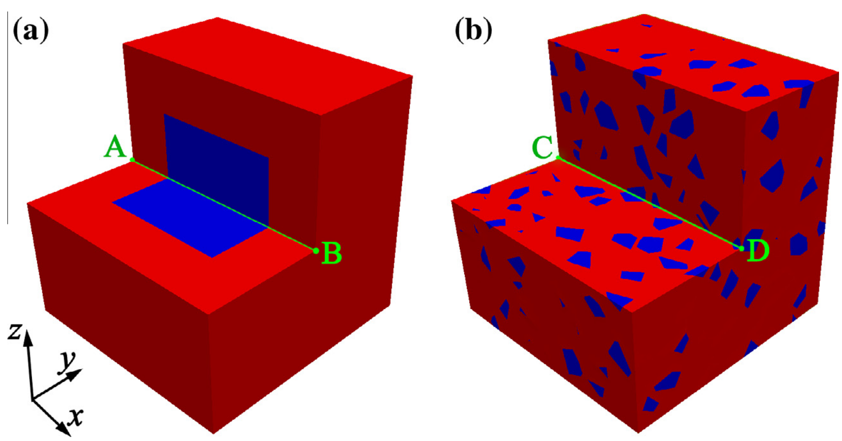

Fig. 12. Position and direction of lines in the microstructures along which the residual stresses will be analyzed: (a) line $\overline{AB}$ across the center of UC along the *x* direction, (b) line $\overline{CD}$ across the center of VE20 along the *x* direction.

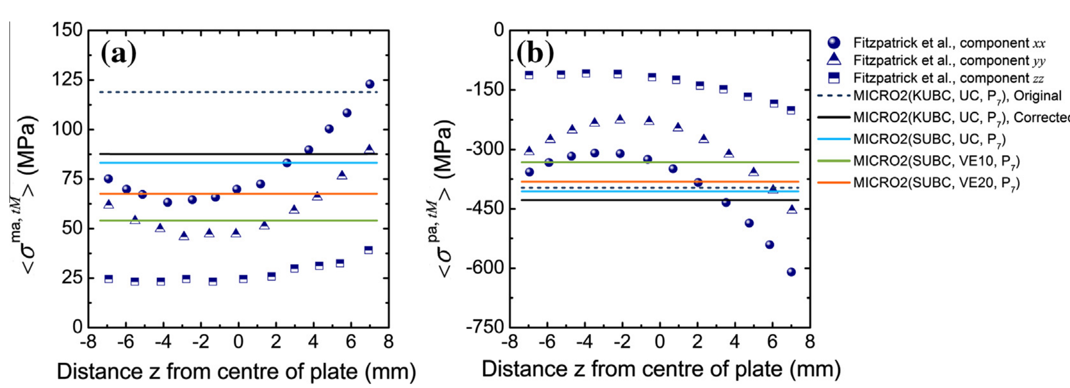

Fig. 13. Comparison between the homogenized thermal misfit residual stresses via different microscale models and the determined ones via Eshelby model from Fitzpatrick et al. [11] in 2124Al (a) and SiC (b).

Fig. 11(c) and (d) indicate that the variation trend and nature of $\sigma_{zz}^{\mathrm{pa},eM}$ are contrary to those of $\sigma_{xx}^{\mathrm{pa},eM}$ and $\sigma_{yy}^{\mathrm{pa},eM}$ in many areas of particles. This reveals that the microscale models based on UC introduce significant errors in the computation of microscale stress

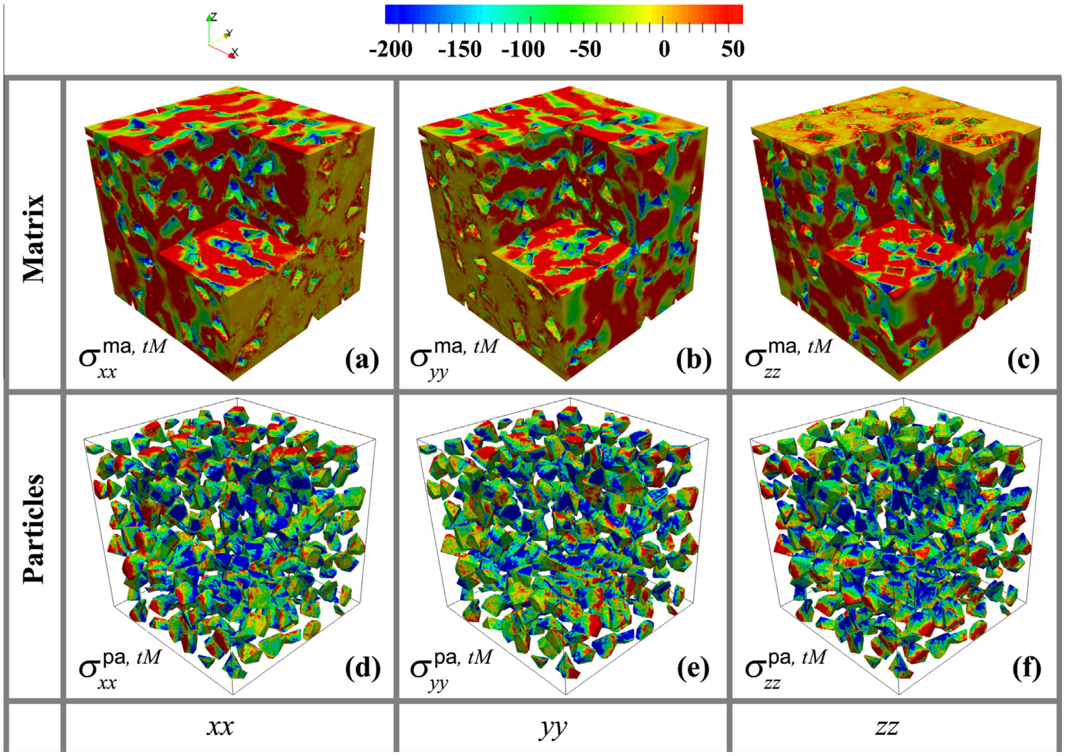

Fig. 14. Thermal misfit plus plastic misfit residual stress fields computed via MICRO2(SUBC, VE20, P_7).

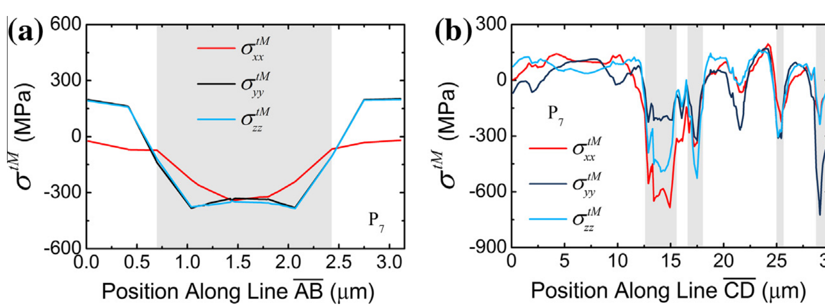

Fig. 15. Thermal misfit plus plastic misfit residual stress that computed via (a) MICRO2(SUBC, UC, P_7) and (b) MICRO2(SUBC, VE20, P_7).

field compared with those based on the large sized realistic microstructure models.

4.5. Thermal misfit residual stress

Fig. 13 shows the homogenized thermal misfit residual stresses computed via different microscale models and the determined ones based on Eshelby model [11]. The thermal misfit residual stress is expected to be isotropic, because the orientation of the reinforcement is random. It can be seen that the determined $\langle\sigma_i^{\beta,tM}\rangle$ based on Eshelby model are obviously anisotropic [11]. In the simulations, some anisotropy of the predicted thermal misfit residual stress will be observed because of the little anisotropy of the 3D realistic microstructure models with finite domain size. In the present work, the variations between different components of $\langle\sigma_i^{\mathrm{ma},tM}\rangle$ are 0.07, 0.46, 3.16 and 0.46 MPa and those of $\langle\sigma_i^{\mathrm{pa},tM}\rangle$ are 5.10, 2.27, 19.44 and 2.26 MPa for MICRO2(KUBC, UC, P_7), MICRO2(SUBC, UC, P_7), MICRO2(SUBC, VE10, P_7), and MICRO2 (SUBC, VE20, P_7), respectively.

The significant variations between different components of $\langle\sigma_i^{\beta,tM}\rangle$ in MICRO2(SUBC, VE10, P_7) can be explained by the anisotropy of the microstructure of VE10. In VE10, only 44 particles are included as shown in Fig. 1. With this small number of particles, the anisotropy of the 3D microstructure of VE10 cannot be ignored. In VE20, 408 particles are included and the isotropy of VE20 is better than that of VE10. As a return, the accuracy of the computed thermal misfit residual stress is improved.

In order to show $\langle\sigma_i^{\beta,tM}\rangle$ more clearly, the mean homogenized thermal misfit residual stresses are shown in Fig. 13. It can be seen that various boundary conditions have significant influences on the predicted $\langle\sigma_i^{\beta,tM}\rangle$. With changing the KUBC to the SUBC, based on UC, $\langle\sigma_i^{\mathrm{ma},tM}\rangle$ changes from 118.95 to 83.24 MPa with a deviation of ~43% and $\langle\sigma_i^{\mathrm{pa},tM}\rangle$ changes from −396.79 to −406.39 MPa with a deviation of ~2%. As reported in the previous work [31], the KUBC

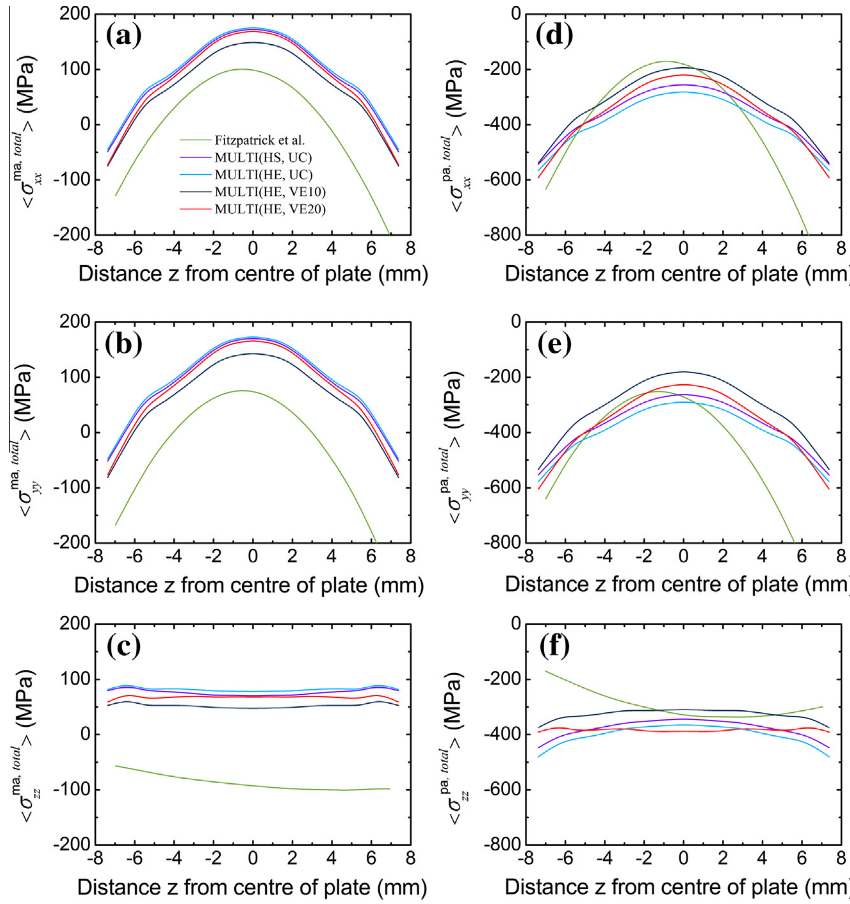

Fig. 16. Comparison between the computed total residual stresses and the experimental ones from Fitzpatrick et al. [11] in 2124Al and SiC.

impose undesirable constraints and leads to ghost forces on the boundary surfaces of the microscale models, i.e. $\langle\sigma_i^{tM}\rangle \neq 0$, where

$$\langle\sigma_i^{tM}\rangle = \frac{1}{\omega}\int_{\omega}\sigma_i^{\beta,tM}d\omega. \tag{5}$$

Subtracting the $\langle\sigma_i^{tM}\rangle$ from $\langle\sigma_i^{\mathrm{ma},tM}\rangle$ and $\langle\sigma_i^{\mathrm{pa},tM}\rangle$, then the corrected $\langle\sigma_i^{\mathrm{ma},tM}\rangle$ and $\langle\sigma_i^{\mathrm{pa},tM}\rangle$ predicted via MICRO2(KUBC, UC, P_7) are 87.67 and −428.06 MPa, respectively, which are very close to the those predicted via MICRO2(SUBC, UC, P_7), as shown in Fig. 13(a) and (b).

With the SUBC, $\boldsymbol{t}_m = \mathbf{0}$ is set for the boundary surfaces, which guaranties that there are no ghost forces on the boundary surfaces. It is found that $\langle\sigma_i^{tM}\rangle$ holds 54.7, 0, 0 and 0 MPa for UC with the KUBC, UC with the SUBC, VE10 with the SUBC and VE20 with the SUBC, respectively. This reveals that by applying the SUBC the ghost force problem is solved.

As shown in Fig. 13(a) and (b), 0.17 × (−406.39) + (1.0–0.17) × 83.24 MPa = 0 MPa holds for UC with the SUBC. However, 0.17 × (−332.52) + (1.0–0.17) × 54.06 MPa = −11.66 MPa is for VE10 with the SUBC; and 0.17 × (−381.80) + (1.0–0.17) × 67.60 MPa = −8.80 MPa is for VE20 with the SUBC. These indicate that by applying the SUBC the equilibrium condition of microscopic stresses (ECMS) between the two phases are still not guaranteed, although the ghost force problem can be solved. Such a new problem is probably caused by the anisotropy of the 3D microstructures of VE10 and VE20. UC is isotropic along the *x*, *y* and *z* direction, so ECMS holds; but VE10 (44 particles are included) is slightly anisotropic along the *x*, *y* and *z* direction, so ECMS does not hold. The isotropy of VE20 (408 particles are included) is better than that of VE10, so the variation of ECMS for VE20 is also reduced. Therefore, increasing the size of microstructure, the variation of the predicted thermal misfit residual stress decreases and the results are getting closer and closer to the real values.

In this study, non-periodic realistic microstructures are employed in the volume elements and interface-aligned non-regular finite element meshes for the discretization are used. The surface meshes on opposite faces of the volume element are not aligned in general. In this case, the discretization of periodic boundary conditions (PBC) is more difficult than that of KUBC and SUBC. Also the iterative solution of the linear system and the parallelization of the algorithms are difficult for PBC. Therefore, the PBC were not considered in this study. For PBC there are other efficient numerical methods, which use regular grids and the fast Fourier transform (FFT), see e.g. [28]. However, one disadvantage of the latter methods is the worse approximation of both material interfaces and the solution at these interfaces. Furthermore, the advantage of KUBC and SUBC is that they predict upper and lower bounds of the effective property. These bounds converge to the correct value for increasing sizes of the volume elements. In other words, if the difference between the solutions with respect to the KUBC and SUBC is too high, then the size of the volume element has to be increased.

Fig. 14 visualizes the thermal misfit residual stress fields. It confirms that the stress fields are approximately isotropic. Fig. 15 shows the profiles of $\sigma_i^{\beta,tM}$ along the line $\overline{AB}$ in microscale model UC and the line $\overline{CD}$ in the microscale model P_7. Fig. 15(a) shows local anisotropy of the stress fields of $\sigma_i^{\beta,tM}$. Especially, Fig. 15(a) shows that $\sigma_{xx}^{\mathrm{ma},tM}$ is locally compressive along the line $\overline{AB}$, while the mean value $\langle\sigma_{xx}^{\mathrm{ma},tM}\rangle$ is tensile. Fig. 15(b) shows that the profiles

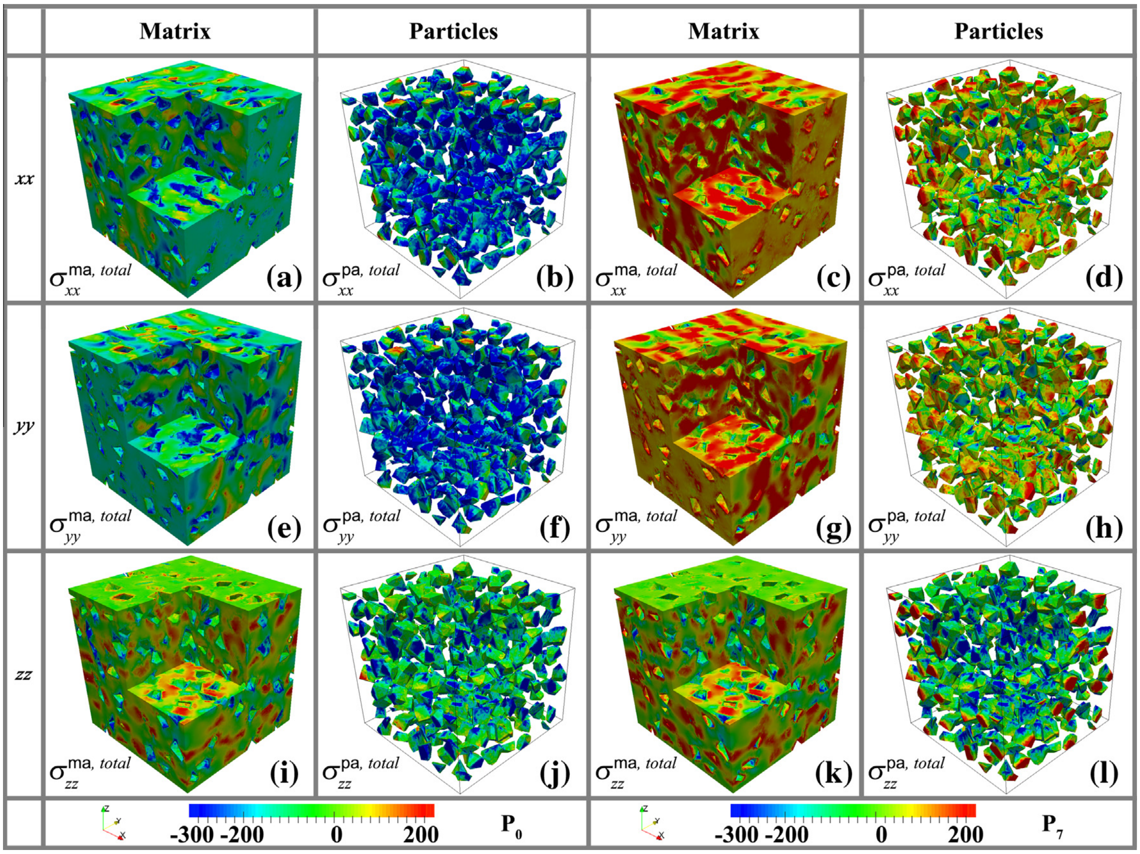

Fig. 17. Total residual stress fields computed based on VE20: the left two rows, i.e. (a), (b), (e), (f), (i) and (j), are the total stress fields for point P0; the right two rows, i.e. (c), (d), (g), (h), (k) and (l), are the total stress fields for point P_7.

of $\sigma_i^{\beta,tM}$ look like 'random', but they are not real random. The local values $\sigma_i^{\beta,tM}$ depend on the CTE of both phases and the morphological features of particles. $\sigma_i^{\mathrm{ma},tM}$ near the matrix/particle interface are low tensile values or compressive values, whereas they are tensile in the area away from the matrix/particle interface as it should be.

Fig. 15(a) shows that the maximum magnitude of $\sigma_i^{\mathrm{pa},tM}$ computed via MICRO2(SUBC, UC, P_7) is close to the mean value $\langle\sigma_i^{\mathrm{pa},tM}\rangle$ as shown in Fig. 13(b). Differently, Fig. 15(b) shows that the maximum magnitude of $\sigma_i^{\mathrm{pa},tM}$ computed via MICRO2(SUBC, VE20, P_7) can be as large as twice of the mean value $\langle\sigma_i^{\mathrm{pa},tM}\rangle$ as shown in Fig. 13(b). This again reveals that the microscale models based on the unit cell model result in unreliable local stress at microscale compared to those based on the large sized realistic microstructure models.

4.6. Total residual stress

Fig. 16(a)–(c) show that MULTI(HE, UC) gives the upper bound of $\langle\sigma_i^{\mathrm{ma},total}\rangle$, while MULTI(HE, VE10) gives the lower bound of $\langle\sigma_i^{\mathrm{ma},total}\rangle$. Fig. 16(a) and (b) show that the total variation of $\langle\sigma_{xx}^{\mathrm{ma},total}\rangle$ or $\langle\sigma_{yy}^{\mathrm{ma},total}\rangle$ predicted via MULTI(HE, VE20) is ~242 MPa, and is ~20 MPa larger than those computed via MULTI(HE, UC) and MULTI(HE, VE10).

Fig. 16(d)–(f) show that MULTI(HE, VE10) gives the upper bound of $\langle\sigma_i^{\mathrm{pa},total}\rangle$; the profiles of $\langle\sigma_i^{\mathrm{pa},total}\rangle$ computed via MULTI (HE, VE20) intersect those computed via MULTI(HS, UC) and MULTI(HE, UC). Fig. 16(d) and (e) show that the total variation of $\langle\sigma_{xx}^{\mathrm{pa},total}\rangle$ or $\langle\sigma_{yy}^{\mathrm{pa},total}\rangle$ computed via MULTI(HE, VE20) is ~372 MPa, and is ~87 and ~27 MPa larger than those computed via MULTI (HE, UC) and MULTI(HE, VE10), respectively.

The $\sigma_i^{\beta,total}$ fields at points P_0 and P_7 are visualized in Fig. 17. To obtain the exact values at different positions, the total residual stress components along the line $\overline{AB}$ that are computed via MICRO1(HE, UC, P_0) and those along the line $\overline{CD}$ that are computed via microscale models MICRO1(HE, VE20, P_0) are shown in Figs. 18 and 19. The profiles of macroscopic, elastic mismatch, thermal misfit residual stresses are also compared with the total residual stress as shown in Figs. 18 and 19.

Figs. 18 and 19 show that the profiles and total variations of $\sigma_i^{\beta,total}$ are dominated by those of the thermal misfit residual stress at the microscale. This is interesting because at the macroscale, the profiles and total variations of $\langle\sigma_i^{\beta,total}\rangle$ across the thickness of the MMC plate are dominated by those of the macroscopic residual stress for this quenching process [11,31]. Differently, for the friction stir welding of MMCs, the profiles and total variations of $\langle\sigma_i^{\beta,total}\rangle$ across the weld at the macroscale are dominated by those of the macroscopic residual stress in the matrix, and by those of the elastic mismatch residual stress in the reinforcement [12].

4.7. Numerical aspects

The Newton–Raphson (NR) iteration method was applied on both the macroscale and microscale to solve the hierarchical multiscale model and hybrid-semiconcurrent multiscale model. In the NR iteration method, the number of NR iterations which reflects the computational efficiency is one of the most important items of the numerical aspects.

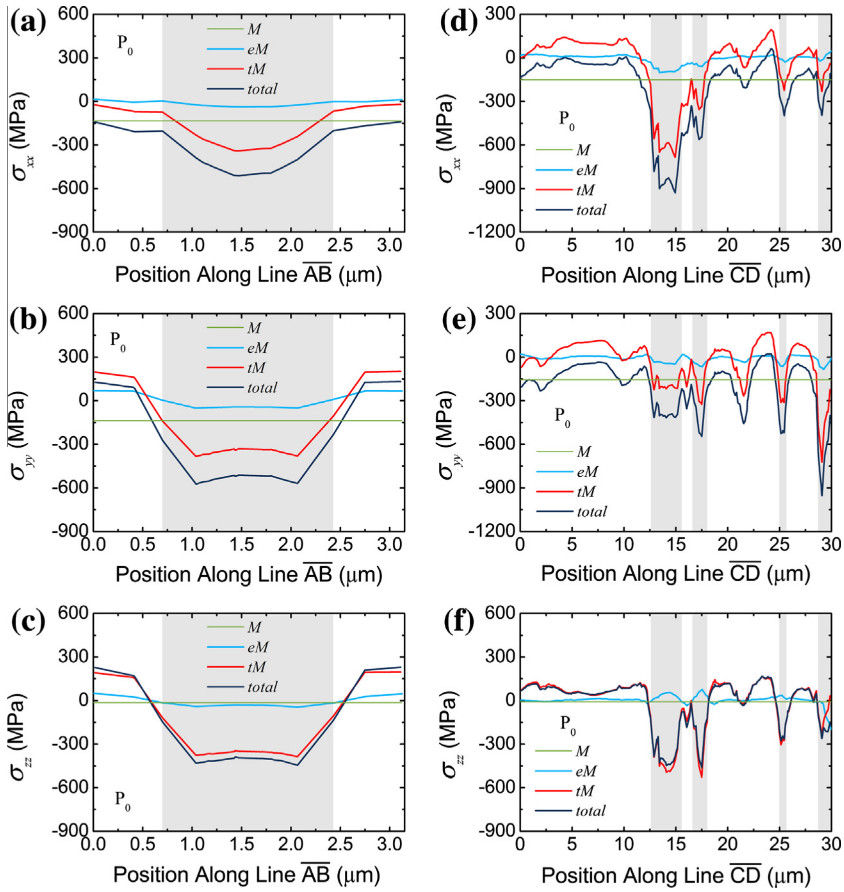

Fig. 18. Macroscopic, elastic mismatch, thermal misfit and total residual stresses along the line $\overline{AB}$ (a)–(c) and line $\overline{CD}$ (d)–(f) for the top surface of the real MMC plate. M: macroscopic residual stress; eM: elastic mismatch residual stress; tM: thermal misfit residual stress; total: total residual stress.

Table 3 compares the numbers of NR iterations for the mechanical part between the hybrid-semiconcurrent and hierarchical multiscale models based on UC. The stopping criterion is 1.0E−5 and 1.0E−6 for NR at the macroscale and the microscale, respectively. Table 3 clearly shows that the hierarchical multiscale model is more efficient than the hybrid-semiconcurrent one. Based on UC, the number of NR iterations for the macroscale and microscale models of the hierarchical multiscale model is about 96% and 33–36%, respectively, of those of the hybrid-semiconcurrent multiscale model. More details about the NR iterations of the macroscale model and the microscale model for both the hierarchical and hybrid-semiconcurrent multiscale models are shown in the supplementary data. It can be seen that the hierarchical multiscale model shows great improvement of the computational efficiency compared with the hybrid-semiconcurrent multiscale model.

Besides the number of NR iterations, the degree of freedom (DOF) of one model which reflects the computational cost is another most important item of the numerical aspects. The larger DOF, the larger computer memory is required for solving the model. For thermo-mechanical models, the maximum computer memory is determined by the DOF of the mechanical part.

In the mechanical part of both the hierarchical and hybrid-semiconcurrent multiscale models, the mesh nodes of the macroscale model are 21,290 with 63,870 DOF, while the mesh nodes of one microscale UC model are 1339 with 4017 DOF. In the hierarchical multiscale models, the mesh nodes of the microscale models based on VE10 and VE20 are 102,339 and 786,677, respectively, with the 307,017 and 2,360,031 DOFs for the mechanical parts, respectively. Based on these numbers, it is easy to calculate that if VE20 is applied in the hybrid-semiconcurrent multiscale model, then the total DOF is $2{,}360{,}031 \times 8 + 63{,}870 = 18{,}944{,}118$.

In the hierarchical multiscale models, the microscale models and the macroscale model are decoupled from the view of solution scheme. Therefore, the DOF of the hierarchical multiscale models only depends on single scale model. For instance, for the VE20 based hierarchical multiscale model, the maximum DOF during the solution process is 2,360,031.

The used computer memory for solving MULTI(HS, UC) with points P_0–P_7 is ~732 MB, MACRO(UC, P_0) ~530 MB, MICRO1(HE, UC, P_0) ~31 MB, MICRO2(SUBC, UC, P_7) ~35 MB, MICRO1(HE, VE20, P_0) ~19 GB, MICRO2(SUBC, VE20, P_7) ~21 GB. Using these data, the required computer memory for solving MULTI(HS, VE20) with points P_0–P_7 can be approximately calculated by $530\ \text{MB} + 19\ \text{GB} \times 8\ \text{Points} \approx 153\ \text{GB}$, which indicates that MULTI (HS, VE20) with points P_0–P_7 is difficult to be solved in a standard workstation.

Therefore, it can be seen that the hierarchical multiscale model gains significant advantages over the hybrid-semiconcurrent one from the view of numerical aspects.

5. Conclusions

The work presents a hierarchical multiscale method for predicting accurately and efficiently the macroscopic and microscopic residual stresses in MMCs based on realistic digital microstructure models. The effects of various modeling conditions on the results and numerical aspects are discussed. The following conclusions can be made.

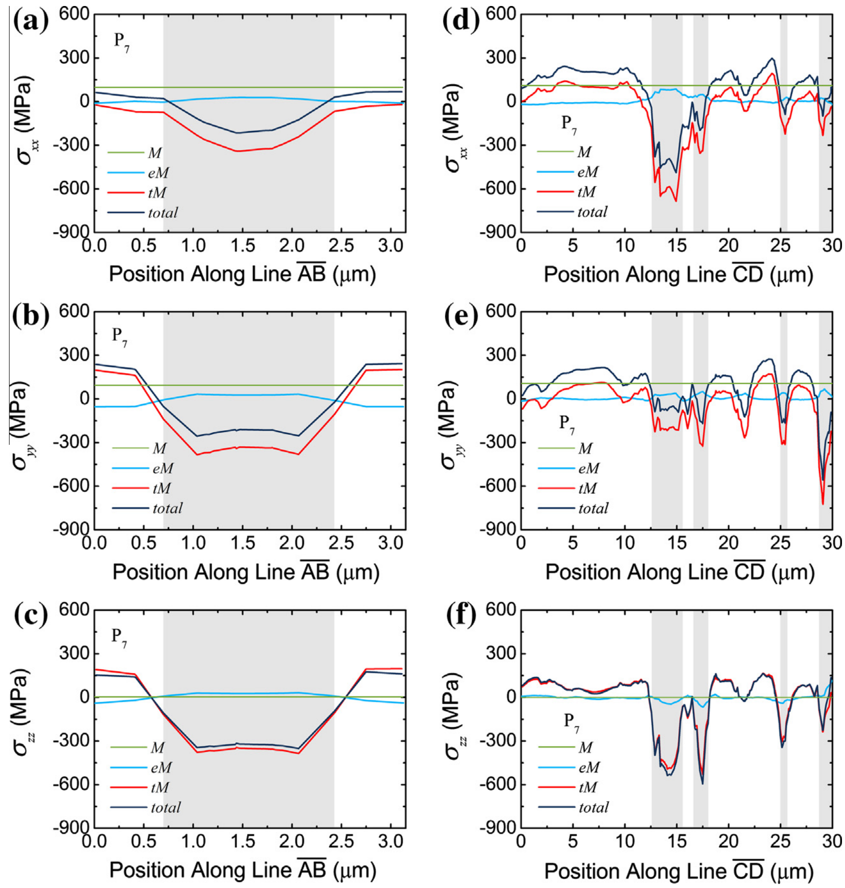

Fig. 19. Macroscopic, elastic mismatch, thermal misfit and total residual stresses along the line $\overline{AB}$ (a)–(c) and line $\overline{CD}$ (d)–(f) for the center of the real MMC plate.

Table 3
Comparison in statistics of NR iterations between hybrid-semiconcurrent (HS) and hierarchical (HE) multiscale models based on UC.

Type of multiscale model	NR iterations on the macroscale	NR iterations on the microscale models at different points							
		P_0	P_1	P_2	P_3	P_4	P_5	P_6	P_7
HS	1394	3695	3567	3353	3313	3462	3514	3524	3474
HE	1335	1226	1194	1195	1203	1198	1202	1204	1205
Ratio*	96%	33%	33%	36%	36%	35%	34%	34%	35%

* Ratio = NR iterations of hierarchical type multiscale model ÷ NR iterations of hybrid-semiconcurrent type multiscale model × 100%.

1. The hierarchical multiscale model shows good self-consistency and good accuracy, where the homogenized macroscopic residual stress via microscale models agrees very well with the directly predicted one via the macroscale model. Based on the same microstructure, the hierarchical multiscale model predicts almost the same macroscopic residual stress with the hybrid-semiconcurrent multiscale model.
2. For accurate multiscale modeling, large size realistic microstructure model should be used. Unit cell based multiscale model greatly underestimates the total variations of $\langle\sigma_{xx}^{\beta,eM}\rangle$ and $\langle\sigma_{yy}^{\beta,eM}\rangle$ across the thickness of the MMC plate. With the hierarchical coupling method, the larger domain size of the realistic microstructure, the larger total variations of $\langle\sigma_{xx}^{\beta,eM}\rangle$ and $\langle\sigma_{yy}^{\beta,eM}\rangle$ across the thickness of the MMC plate. The total variations of $\langle\sigma_{xx}^{\beta,eM}\rangle$ and $\langle\sigma_{yy}^{\beta,eM}\rangle$ predicted via hierarchical multiscale model based on VE20 agree with the experimental results very well.
3. The macro–micro transition boundary conditions, i.e. the KUBC and the SUBC, have significant effects on the predicted thermal misfit residual stress. In all the microscale models, the SUBC successively avoids the ghost force problem on the boundary surfaces. The size of the volume element has significant effects on the predicted thermal misfit residual stress.
4. The unit cell based multiscale models introduce significant errors in the predictions of the microscopic residual stresses. The realistic microstructure based hierarchical multiscale model gives better approximations of the microscopic residual stresses, i.e. the elastic mismatch, thermal misfit residual stresses, which provide deep insight into the microscopic residual stresses. For accurate prediction of microscopic residual stresses, the realistic microstructure is required.
5. The local fluctuation profiles and the total variations of the total residual stress are dominated by those of the thermal misfit residual stress at the microscale, which is quite different from the status at the macroscale. The profiles and the total variations of the total residual stress are dominated by those of the macroscopic residual stress at the macroscale.
6. The hierarchical multiscale model gains significant advantages over the hybrid-semiconcurrent with respect to the numerical

effort. Based on UC, the number of NR iterations for the macroscale and microscale models of the hierarchical multiscale model is about 96% and 33–36%, respectively, of those of the hybrid-semiconcurrent multiscale model. The computer memory cost is significantly reduced for solving hierarchical multiscale models compared with hybrid-semiconcurrent multiscale models.

Acknowledgments

The authors gratefully acknowledge support from the National Natural Science Foundation of China under Grant No. 51401219 and the National Basic Research Program of China under Grant No. 2012CB619600. The authors would like to thank Prof. P.J. Withers for his helpful discussions and comments.

Appendix A. Supplementary data

Supplementary data associated with this article can be found, in the online version, at http://dx.doi.org/10.1016/j.compstruct.2015.10.045.

References

[1] Withers PJ. Residual stress and its role in failure. Rep Prog Phys 2007;70:2211–64.
[2] Arsenault RJ, Taya M. Thermal residual-stress in metal matrix composite. Acta Metall 1987;35:651–9.
[3] Ho S, Lavernia EJ. Thermal residual stresses in metal matrix composites: a review. Appl Compos Mater 1995;2:1–30.
[4] Fernandez R, Bruno G, Gonzalez-Doncel G. Correlation between residual stresses and the strength differential effect in PM 6061Al-15 vol% SiCw composites: experiments, models and predictions. Acta Mater. 2004;52:5471–83.
[5] Schobel M, Baumgartner G, Gerth S, Bernardi J, Hofmann M. Microstresses and crack formation in AlSi7MgCu and AlSi17Cu4 alloys for engine components. Acta Mater 2014;81:401–8.
[6] Ni DR, Chen DL, Xiao BL, Wang D, Ma ZY. Residual stresses and high cycle fatigue properties of friction stir welded SiCp/AA2009 composites. Int J Fatigue 2013;55:64–73.
[7] Liljedahl CDM, Brouard J, Zanellato O, Lin J, Tan ML, Ganguly S, et al. Weld residual stress effects on fatigue crack growth behaviour of aluminium alloy 2024–T351. Int J Fatigue 2009;31:1081–8.
[8] Ma YE, Staron P, Fischer T, Irving PE. Size effects on residual stress and fatigue crack growth in friction stir welded 2195-T8 aluminium – Part I: Experiments. Int J Fatigue 2011;33:1417–25.
[9] Biallas G. Effect of welding residual stresses on fatigue crack growth thresholds. Int J Fatigue 2013;50:10–7.
[10] Marschall CW, Maringer RE. Dimensional instability: an introduction. 1st ed. Oxford: Pergamon Press; 1977.
[11] Fitzpatrick ME, Hutchings MT, Withers PJ. Separation of macroscopic, elastic mismatch and thermal expansion misfit stresses in metal matrix composite quenched plates from neutron diffraction measurements. Acta Mater 1997;45:4867–76.
[12] Zhang XX, Ni DR, Xiao BL, Andrä H, Gan WM, Hofmann M, et al. Determination of macroscopic and microscopic residual stresses in friction stir welded metal matrix composites via neutron diffraction. Acta Mater 2015;87:161–73.
[13] Withers PJ, Preuss M, Steuwer A, Pang JWL. Methods for obtaining the strain-free lattice parameter when using diffraction to determine residual stress. J Appl Crystallogr 2007;40:891–904.
[14] Denton AR, Ashcroft NW. Vegard's law. Phys Rev A 1991;43:3161–4.
[15] Eshelby JD. The determination of the elastic field of an ellipsoidal inclusion, and related problems. Proc R Soc Lon Ser-A 1957;241:376–96.
[16] Kroner E. Berechnung der elastischen konstanten des vielkristalls aus den konstanten des einkristalls. Z Phys 1958;151:504–18.
[17] Withers PJ, Stobbs WM, Pedersen OB. The application of the Eshelby method of internal-stress determination to short fiber metal matrix composites. Acta Metall 1989;37:3061–84.
[18] Povirk GL, Stout MG, Bourke M, Goldstone JA, Lawson AC, Lovato M, et al. Thermally and mechanically induced residual strains in Al–SiC composites. Acta Metall Mater 1992;40:2391–412.
[19] Davis LC, Allison JE. Residual-stresses and their effects on deformation in particle-reinforced metal-matrix composites. Metall Trans A 1993;24:2487–96.
[20] Ho S, Saigal A. Three-dimensional modelling of thermal residual stresses and mechanical behavior of cast SiC/Al particulate composites. Acta Metall Mater 1994;42:3253–62.
[21] Schmauder S, Weber U, Soppa E. Computational mechanics of heterogeneous materials – influence of residual stresses. Comput Mater Sci 2003;26:142–53.
[22] Bouafia F, Serier B, Bouiadjra BAB. Finite element analysis of the thermal residual stresses of SiC particle reinforced aluminum composite. Comput Mater Sci 2012;54:195–203.
[23] Golanski D, Terada K, Kikuchi N. Macro and micro scale modeling of thermal residual stresses in metal matrix composite surface layers by the homogenization method. Comput Mech 1997;19:188–202.
[24] Feyel F. Multiscale FE^2 elastoviscoplastic analysis of composite structures. Comput Mater Sci 1999;16:344–54.
[25] Doghri I, Ouaar A. Homogenization of two-phase elasto-plastic composite materials and structures – study of tangent operators, cyclic plasticity and numerical algorithms. Int J Solids Struct 2003;40:1681–712.
[26] Kanoute P, Boso DP, Chaboche JL, Schrefler BA. Multiscale methods for composites: a review. Arch Comput Method Eng 2009;16:31–75.
[27] Llorca J, Gonzalez C, Molina-Aldareguia JM, Segurado J, Seltzer R, Sket F, et al. Multiscale modeling of composite materials: a roadmap towards virtual testing. Adv Mater 2011;23:5130–47.
[28] Spahn J, Andrä H, Kabel M, Muller R. A multiscale approach for modeling progressive damage of composite materials using fast Fourier transforms. Comput Method Appl Mech Eng 2014;268:871–83.
[29] Weinan E, Engquist B, Li XT, Ren WQ, Vanden-Eijnden E. Heterogeneous multiscale methods: a review. Commun Comput Phys 2007;2:367–450.
[30] Belytschko T, Song JH. Coarse-graining of multiscale crack propagation. Int J Numer Meth Eng 2010;81:537–63.
[31] Zhang XX, Xiao BL, Andrä H, Ma ZY. Multi-scale modeling of the macroscopic, elastic mismatch and thermal misfit stresses in metal matrix composites. Compos Struct 2015;125:176–87.
[32] Ghosh S, Lee K, Raghavan P. A multi-level computational model for multi-scale damage analysis in composite and porous materials. Int J Solids Struct 2001;38:2335–85.
[33] Feyel F. Application du calcul parallèle aux modèles à grand nombre de variables internes [Thèse de doctorat]. Ecole Nationale Supérieure des Mines de Paris; 1998.
[34] Özdemir I, Brekelmans WAM, Geers MGD. FE^2 computational homogenization for the thermo-mechanical analysis of heterogeneous solids. Comput Method Appl Mech Eng 2008;198:602–13.
[35] Jung JM, Yoo JH, Jeong HJ, Lee S, Kim HS. Three-dimensional characterization of SiC particle-reinforced Al composites using serial sectioning tomography and thermo-mechanical finite element simulation. Metall Mater Trans A 2014;45A:5679–90.
[36] van der Sluis O, Schreurs PJG, Brekelmans WAM, Meijer HEH. Overall behaviour of heterogeneous elastoviscoplastic materials: effect of microstructural modelling. Mech Mater 2000;32:449–62.
[37] Terada K, Hori M, Kyoya T, Kikuchi N. Simulation of the multi-scale convergence in computational homogenization approaches. Int J Solids Struct 2000;37:2285–311.
[38] Ostoja-Starzewski M. Material spatial randomness: From statistical to representative volume element. Probab Eng Eng Mech 2006;21:112–32.
[39] Gitman IM, Askes H, Sluys LJ. Representative volume: existence and size determination. Eng Fract Mech 2007;74:2518–34.
[40] Zhang XX, Xiao BL, Andrä H, Ma ZY. Homogenization of the average thermo-elastoplastic properties of particle reinforced metal matrix composites: the minimum representative volume element size. Compos Struct 2014;113:459–68.
[41] Laurence B. Homogenization of elasto-(visco)plastic composites: history-dependent incremental and variational approaches [Ph.D. thesis]. Université catholique de Louvain; 2011.
[42] Zhang XX, Zhang Q, Zangmeister T, Xiao BL, Andrä H, Ma ZY. A three-dimensional realistic microstructure model of particle-reinforced metal matrix composites. Modell Simul Mater Sci Eng 2014;22:035010 [21 pages].
[43] Aerospace structural metals database. <https://cindasdata.com/Applications/ASMD/?subaction=reload%3Amcode&mname=2124&mcode=3221>.
[44] Munro RG. Material properties of a sintered alpha-SiC. J Phys Chem Ref Data 1997;26:1195–203.
[45] Si H. TetGen a quality tetrahedral mesh generator and three-dimensional delaunay triangulator. 1.4 ed.; 2006.
[46] Mura T. Micromechanics of defects in solids. 2nd ed. Netherlands: Springer; 1987.
[47] Fitzpatrick ME, Withers PJ, Baczmanski A, Hutchings MT, Levy R, Ceretti M, et al. Changes in the misfit stresses in an Al/SiC_p metal matrix composite under plastic strain. Acta Mater 2002;50:1031–40.
[48] Taya M, Lulay KE, Lloyd DJ. Strengthening of a particulate metal matrix composite by quenching. Acta Metall Mater 1991;39:73–87.
[49] Ramakrishnan N. An analytical study on strengthening of particulate reinforced metal matrix composites. Acta Mater 1996;44:69–77.
[50] Vogelsang M, Arsenault RJ, Fisher RM. An in situ HVEM study of dislocation generation at Al/SiC interfaces in metal matrix composites. Metall Trans A 1986;17:379–89.
[51] Chobaut N, Carron D, Arsene S, Schloth P, Drezet JM. Quench induced residual stress prediction in heat treatable 7xxx aluminium alloy thick plates using Gleeble interrupted quench tests. J Mater Process Technol 2015;222:373–80.
[52] Mesarovic SD, Padbidri J. Minimal kinematic boundary conditions for simulations of disordered microstructures. Philos Mag 2005;85:65–78.